Received: 28 September 2023 | Revised: 9 February 2024 | Accepted: 23 February 2024

DOI: 10.1002/mp.17024

RESEARCH ARTICLE

MEDICAL PHYSICS

Experimental demonstration of real-time cardiac physiology-based radiotherapy gating for improved cardiac radioablation on an MR-linac

Osman Akdag[1] | **Pim T. S. Borman**[1] | **Stefano Mandija**[1,2] | **Peter L. Woodhead**[1,3] | **Prescilla Uijtewaal**[1] | **Bas W. Raaymakers**[1] | **Martin F. Fast**[1]

[1]Department of Radiotherapy, University Medical Center Utrecht, Utrecht, The Netherlands

[2]Computational Imaging Group for MR Diagnostics and Therapy, Center for Image Sciences, University Medical Center Utrecht, Utrecht, The Netherlands

[3]Elekta AB, Stockholm, Sweden

Correspondence
Osman Akdag and Martin F. Fast, Department of Radiotherapy, University Medical Center Utrecht, Heidelberglaan 100, 3584 CX Utrecht, The Netherlands.
Email: o.akdag-3@umcutrecht.nl and m.f.fast-2@umcutrecht.nl

Funding information
Nederlandse Organisatie voor Wetenschappelijk Onderzoek, Grant/Award Number: 17 515

Abstract

Background: Cardiac radioablation is a noninvasive stereotactic body radiation therapy (SBRT) technique to treat patients with refractory ventricular tachycardia (VT) by delivering a single high-dose fraction to the VT isthmus. Cardiorespiratory motion induces position uncertainties resulting in decreased dose conformality. Electocardiograms (ECG) are typically used during cardiac MRI (CMR) to acquire images in a predefined cardiac phase, thus mitigating cardiac motion during image acquisition.

Purpose: We demonstrate real-time cardiac physiology-based radiotherapy beam gating within a preset cardiac phase on an MR-linac.

Methods: MR images were acquired in healthy volunteers (n = 5, mean age = 29.6 years, mean heart-rate (HR) = 56.2 bpm) on the 1.5 T Unity MR-linac (Elekta AB, Stockholm, Sweden) after obtaining written informed consent. The images were acquired using a single-slice balance steady-state free precession (bSSFP) sequence in the coronal or sagittal plane (TR/TE = 3/1.48 ms, flip angle = 48°, SENSE = 1.5, field-of-view = 400×207 mm^2, voxel size = $3 \times 3 \times 15$ mm^3, partial Fourier factor = 0.65, frame rate = 13.3 Hz). In parallel, a 4-lead ECG-signal was acquired using MR-compatible equipment. The feasibility of ECG-based beam gating was demonstrated with a prototype gating workflow using a Quasar MRI^{4D} motion phantom (IBA Quasar, London, ON, Canada), which was deployed in the bore of the MR-linac. Two volunteer-derived combined ECG-motion traces (n = 2, mean age = 26 years, mean HR = 57.4 bpm, peak-to-peak amplitude = 14.7 mm) were programmed into the phantom to mimic dose delivery on a cardiac target in breath-hold. Clinical ECG-equipment was connected to the phantom for ECG-voltage-streaming in real-time using research software. Treatment beam gating was performed in the quiescent phase (end-diastole). System latencies were compensated by delay time correction. A previously developed MRI-based gating workflow was used as a benchmark in this study. A 15-beam intensity-modulated radiotherapy (IMRT) plan (1×6.25 Gy) was delivered for different motion scenarios onto radiochromic films. Next, cardiac motion was then estimated at the basal anterolateral myocardial wall via normalized cross-correlation-based template matching. The estimated motion signal was temporally aligned with the ECG-signal, which were then used for position- and ECG-based gating simulations in

the cranial–caudal (CC), anterior–posterior (AP), and right–left (RL) directions. The effect of gating was investigated by analyzing the differences in residual motion at 30, 50, and 70% treatment beam duty cycles.

Results: ECG-based (MRI-based) beam gating was performed with effective duty cycles of 60.5% (68.8%) and 47.7% (50.4%) with residual motion reductions of 62.5% (44.7%) and 43.9% (59.3%). Local gamma analyses (1%/1 mm) returned pass rates of 97.6% (94.1%) and 90.5% (98.3%) for gated scenarios, which exceed the pass rates of 70.3% and 82.0% for nongated scenarios, respectively. In average, the gating simulations returned maximum residual motion reductions of 88%, 74%, and 81% at 30%, 50%, and 70% duty cycles, respectively, in favor of MRI-based gating.

Conclusions: Real-time ECG-based beam gating is a feasible alternative to MRI-based gating, resulting in improved dose delivery in terms of high γ-pass rates, decreased dose deposition outside the PTV and residual motion reduction, while by-passing cardiac MRI challenges.

KEYWORDS
cardiac radioablation, gating, MR-linac

1 | INTRODUCTION

Ventricular tachycardia (VT) is a severe cardiac arrhythmia condition in which the ventricles contract at an exceedingly high rate (110–250 beats per minute [bpm]), mainly caused by re-entrant circuits in the myocardium as a result of structural heart disease. VT is managed by the administration of anti-arrhythmic drugs (AAD) or implantable cardioverter-defribillator (ICD) therapy. As a means to permanently terminate VT episodes in VT patients, invasive catheter ablation is the clinical standard. A catheter ablation treatment has procedural limitations and risks, which can lead to complications, recurrence of the arrhythmia condition, or death.[1–4] Cardiac radioablation (CR) or stereotactic arrhythmia radioablation (STAR) has emerged as a promising alternative treatment technique for VT patients.[5,6] STAR is applied by delivering a single high-dose fraction (typically 25 Gy) to the VT isthmus. STAR presents as a highly promising procedure with a major decrease in VT episodes and AAD prescriptions.[7–12]

The treatment target region in the myocardial wall is subject to cardiorespiratory motion that induces position uncertainties, which makes it challenging to achieve a conformal dose delivery.[13] In addition, adjacent organs at risk (OARs) and cardiac substructures are dose sensitive and the cardiorespiratory motion-induced dosimetric uncertainties raise radiation-induced toxicity concerns. Minimizing the treatment target volume and achieving a conformal dose delivery is thus crucial for VT patients.[14–16]

Today, STAR treatments are primarily performed on conventional C-arm or robotic linear accelerators. The target position uncertainties during treatments on these devices are mainly accounted for by respiratory motion management. Equally common strategies are the definition of an internal target volume based on an 4D pre-treatment imaging data set and/or using increased planning target volume (PTV) margins.[17–19]

Alternatively, patients with cardiac treatment targets (e.g., VT isthmuses and cardiac sarcomas) have also been treated on the MR-linac.[20–23] The integration of a linac within an MRI enables superior soft-tissue visualization during radiotherapy and can potentially facilitate the safe reduction of PTVs.[24,25] During these procedures, MRI-guidance may be used to gate the radiation delivery on either a predefined target window or extracardiac structures.[20,26] In a recent experimental study, we demonstrated that the dose delivery can be gated in a predefined cardiac phase in parallel with respiratory MLC-tracking based on real-time 2D cine MRI, which greatly reduced cardiorespiratory motion-induced dosimetric uncertainty.[27] Here, single slice real-time cine MRI was used to capture experimental 1D motion as 3D cardiac motion capturing remains an imaging challenge due to the rapid periodicity of the heart. For clinical applications, the presence of a cardiac implantable electronic device (CIED) in a VT patient increases the imaging challenges as CIEDs induce MRI artefacts and require scan parameter limitations according to MRI safety guidelines.[28–32]

In the cardiac MRI domain, an ECG-signal is utilized to acquire images in a predefined cardiac phase to effectively freeze cardiac motion and acquire images in a stable cardiac anatomy. Recent studies on conventional linacs have shown the feasibility to gate the radiation beam with an intensity modulated radiotherapy (IMRT) and volumetric modulated arc therapy (VMAT) plan in the quiescent periods based on an (a priori known) ECG-signal acquired in real-time. The dosimetric results were improved with respect to an ungated dose delivery and the radiation beam

characteristics remained stable.[33,34] Cardiac-synchronized MRI was recently enabled in research mode on the 1.5 T Unity MR-linac (Elekta AB, Stockholm, Sweden) after installing the clinical Philips MRI ECG equipment (Philips Healthcare, Best, The Netherlands).[35]

In this study, our aim was to investigate the feasibility of cardiac motion mitigation during dose delivery based on an ECG-signal as a cardiac motion surrogate. A prototype adaptive dose delivery workflow was developed in which the installed ECG-equipment was used to gate the radiation beam in the quiescent period of the cardiac cycle in real-time. The ECG-based dose delivery performance was compared with position-based radiation beam gating in terms of system latency, residual motion, and dosimetric performance by conducting film dosimetry experiments in an experimental phantom setup. Additionally, computational simulations were performed for the ECG-based and position-based gating approaches for an effective comparison over a wider variety of ECG-signal and motion traces.

2 | METHODS

2.1 | Experimental setup

All experiments were performed on a 1.5 T Elekta Unity MR-linac. An MR-compatible Quasar MRI^{4D} motion phantom (IBA Quasar, London, ON, Canada) was deployed in the bore of the MR-linac on a support (20° inclination) for film dosimetry experiments. Cables for phantom control and ECG-signal acquisitions were passed through the waveguide to minimize the effect of radiofrequency (RF) noise interference during imaging. The phantom contained a movable spherical treatment target (3-cm diameter) with an intersecting film cassette insert aligned with the coronal plane, which can be moved with 1D translational motion. Radiation beam gating was performed in assumed breath-holds by either using the ECG-signal or MRI-based cardiac position signal (Figure 1) as inputs for radiation beam gating (Section 2.4).

Volunteer-derived 1D cranial–caudal (CC) cardiac motion and ECG-signal (Section 2.3.2) were programmed in the motion phantom using IBA Quasar-provided research software. During ECG-based gating, the motion-synchronized ECG-signal was measured using the Philips 4-lead ECG equipment and received on the client PC using Philips-provided real-time physiology streaming software (Section 2.2.1). Alternatively, for MRI-based gating, the actual position of the treatment target was estimated on cine MR images, which were streamed in real-time using in-house developed software (Section 2.2.2).

2.2 | Beam gating methodologies on the MR-linac

2.2.1 | ECG-based beam-gating

The ECG-signal was used as a cardiac motion surrogate in this approach. The treatment target was moved according to a volunteer-derived cardiac motion pattern (Section 2.3.2), which was synchronized with its corresponding ECG-signal. The control computer of the motion phantom returned the voltage (0–5-V range) via a Bayonet–Neill–Concelman (BNC) connection. The analog voltage output was captured using the Philips MRI 4-lead ECG equipment. The ECG equipment is designed to measure cardiac potentials, which are generally $\mathcal{O}(10^{-1})$ mV. Therefore, a resistive $1:10^4$ voltage divider was used to decrease the output voltage from the motion phantom. Alligator clips were attached on the other end of the coaxial cable adapter to parse the phantom's analog voltage output signal to the Philips MR Host using the ECG equipment (c.f. Figure S-1 in the Appendix).

The recorded voltage output of the motion phantom was streamed in real-time from the Philips MR host in a research software environment to the client PC running on Debian 11 with a quad-core Intel Xeon E3-1240 (Intel Corporation, Santa Clara, USA) and 16-GB memory. The research software included vendor-provided real-time MR physiology reader software in Python and an increased physiology signal streaming frequency of 20 Hz (compared to 5 Hz in clinical mode).

The radiation beam gating decision was made based on the detection of the R-top, which was performed with a Pan–Tompkins-inspired QRS detection algorithm.[36] After R-top detection, the beam-on signal was sent to the gating client after a certain delay time T_d to ensure beam gating in the quiescent phase of the cardiac cycle (Figure 2a). The heart is electrically silent in the quiescent phase (end-diastole) and therefore free from any electric stimuli inducing cardiac motion. With this approach, the residual cardiac motion will be minimized based on the ECG-signal. The absolute gating window duration T_B was prospectively determined based on the average heart rate of the previous three cardiac cycles. A beam-off signal was parsed to the gating client to turn off the beam at the end of the gating window.

2.2.2 | MRI-based beam gating

For comparison purposes, image-derived treatment target positions for radiation beam gating was used similar to our previous study.[27] The treatment target within the motion phantom was moved according to a volunteer-derived cardiac motion pattern (Section 2.3.2). The images of the motion phantom were acquired using

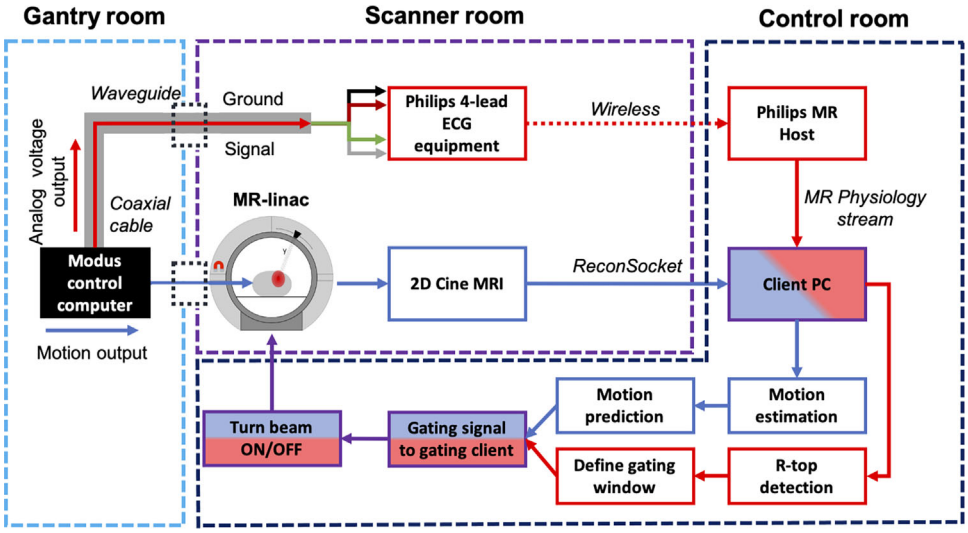

FIGURE 1 A schematic overview of both ECG-based (red arrows) and MRI-based (blue arrows) gating workflows on the MR-linac. The purple components were identical in both workflows.

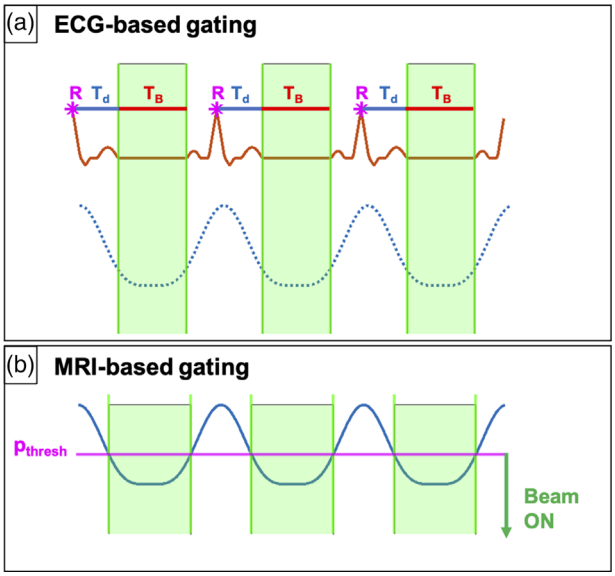

FIGURE 2 (a) A schematic depiction of the ECG-based gating decision-making on a synthetic ECG-signal and its effect on the synchronized artificial position signal. After R-top detection, the beam is turned on after delay time T_d and turned off after beam-on time T_B. Here, T_B is kept constant for display purposes. The dotted line indicates that the motion trace is unknown during ECG-based gating. (b) The MRI-based gating decision-making is shown. The beam is turned on/off when the position threshold, p_{thresh}, is exceeded.

a single-slice 2D balanced steady-state free precession (bSSFP) image acquisition sequence in the sagittal plane (Section 2.3.1) and streamed in real-time to the client PC via ReconSocket.[37] The position of the spherical treatment target was estimated by using the circular Hough transform. The center of the detected circle was then defined as the position of the treatment target. The midposition of the motion trajectory was defined as the threshold, p_{thresh}, for radiation beam gating (Figure 2b).

2.2.3 | System latencies and latency compensation

The ECG- and MRI-based beam gating workflows (Sections 2.2.1 and 2.2.2) are subject to inherent system latencies. The end-to-end system latency was defined as the time difference between the occurrence of a physical event (i.e., phantom motion) and the reaction of the system to act on the event (i.e., gating the radiation beam). The contributors to the end-to-end system latency differ between the ECG- and MRI-based gating approach. The latency for the ECG-based gating approach can be defined as

$$\tau_{ECG} = T_{s_{ECG}} + T_{proc_{ECG}} + T_{gate}, \quad (1)$$

which can be fully compensated under the condition that $\tau_{ECG} < T_d$ (delay time).

Here, $T_{s_{ECG}}$ is the time between recording of the ECG and receiving the ECG on the client PC, $T_{proc_{ECG}}$ the ECG processing time for R-top detection and gating window definition and T_{gate} the necessary time to turn the radiation beam on/off. $T_{s_{ECG}}$ and $T_{proc_{ECG}}$ were measured by programming synthetic ECG signals varying from 50 to 110 bpm in the motion phantom. The phantom's reference voltage output was received via a wired connection on the client PC. This reference voltage output was compared with the phantom's voltage output that was measured via the Philips 4-lead ECG equipment, which was received on the client PC using the real-time MR physiology reader software. The processing times of both received data samples were logged on the client PC and the mean time difference between the R-tops was computed. The estimated end-to-end latency was then subtracted from the delay time T_d during the ECG-based gating workflow.

Similarly, the position-based gating workflow end-to-end latency can be defined as[27]:

$$\tau_{pos} = T_{s_{im}} + T_{proc_{pos}} + T_{gate}. \quad (2)$$

Here, $T_{s_{im}}$ is the average time between acquisition of the k-space center and receiving the image on the client PC and $T_{proc_{pos}}$ the image processing time for position quantification. $T_{s_{im}}$ and $T_{proc_{pos}}$ were estimated by programming sinusoidal trajectories (sin, 5-mm peak-to-peak, 50–110 bpm) in the motion phantom. The phantom's reference positions were compared with the streamed images and processing times were logged.[38] The system latency in the position-based gating workflow was compensated by applying a linear (ridge) regression model,[39] which in prior work was applied to predict respiratory motion[38] and cardiac motion in an experimental setup.[27] Cardiac motion was independently predicted at 146 and 249 ms ahead. The desired position could then be estimated by linear interpolation depending on the current system latency.

2.3 | Image data acquisition and processing

2.3.1 | Study group and data acquisition

Image and ECG-signal data were acquired from a total of five healthy volunteers (mean age = 29.6 years, mean HR = 56.2 bpm) after obtaining written informed consent. For each volunteer, 2D single-slice cine MR images were acquired using the bSSFP imaging sequence (TR/TE = 3/1.48 ms, flip angle = 48°, SENSE = 1.5, field-of-view = 400 × 207 mm^2, voxel size = 3 ×3 × 15 mm^3, partial Fourier factor = 0.65, frame rate = 13.3 Hz). The ECG-signal was recorded during each image acquisition using the Philips MRI 4-lead ECG device.[35] Three cine MRI acquisitions were performed per volunteer. Cine acquisitions of 1000 frames (acquisition time (TA): 1:24 min) were performed in the coronal and sagittal plane. Lastly, a longer (16 384 frames) cine (TA: 20:29 min) was acquired in the sagittal plane only for use during the dosimetry experiments (Section 2.4). The coronal and sagittal image acquisition planes orthogonally intersected each other in the basal anterolateral myocardial wall of the left ventricle.

2.3.2 | Image data processing

The acquired coronal and sagittal cine MR images were used to estimate the CC motion of an artificial cardiac treatment target in the basal anterolateral segment of the myocardial wall (which agrees with segment 6 of the 17-segment left ventricle model[40]). Motion was estimated with normalized cross-correlation-based local rigid registration (i.e., template matching) in Matlab (Mathworks Inc., Natick, MA, USA)[41] using a total of three templates in end-systole, end-diastole, and a cardiac phase in between. During template matching, the preferred template was chosen prospectively based on the highest normalized cross-correlation score. A spatial offset correction between the templates was applied during template matching. The first five seconds of the image data were discarded to ensure that only images were included with an optimal signal for the balanced scan. An artificial rectangular treatment target region (27 × 27 mm^2) was chosen for local motion estimation of the myocardial wall (Figure 3). A heart-rate-tailored band-pass filter was used to isolate the cardiac motion component. The ECG-signal was obtained in a physiology log-file format, which was processed offline in Matlab for synchronization with the obtained cardiac motion component. The synchronized cardiac motion trajectories and ECG-signals were then used as the gating surrogates in our dosimetry experiments.

2.4 | Dosimetry experiments

A 15-beam (83 segments) cardiac stereotactic body radiation therapy (SBRT) treatment plan (1 × 25 Gy) for the Unity MR-linac was created in Monaco v.5.51.10. A 3-mm isotropic PTV margin was used. Film dosimetry experiments were conducted to evaluate the performance of the beam gating workflows. Gafchromic EBT3 (Ashland Advanced Materials, Bridgewater, NJ, USA) dosimetric films were used to measure the delivered dose. The prescription dose was quartered by MU scaling to fit the dynamic range of the dosimetric films. Two volunteer-derived motion traces (n = 2, mean age = 26, mean HR = 57.4, max. peak-to-peak amplitude = 14.7 mm), V1 and V2, were programmed in the motion phantom during the dosimetry experiments in which the dose was delivered with and without gating. These volunteer-derived motion traces were suitable to test the beam gating workflows on a wide range of heart frequencies. As reference, a static dose delivery was performed. The phantom-reported position, ECG-signals, and beam on/off data samples were logged on the client PC with their corresponding timestamps during the gating experiments. The obtained log-files were then processed afterwards to evaluate the gating performances.

2.5 | Dosimetry performance evaluation

2.5.1 | Dosimetric film processing

The dosimetric films were digitized 24 h after irradiation using the Epson Expression 10000XL flatbed scanner (Seiko Epson Corp, Nagano, Japan) with a resolution of 150 dpi. The digitized films were then processed by

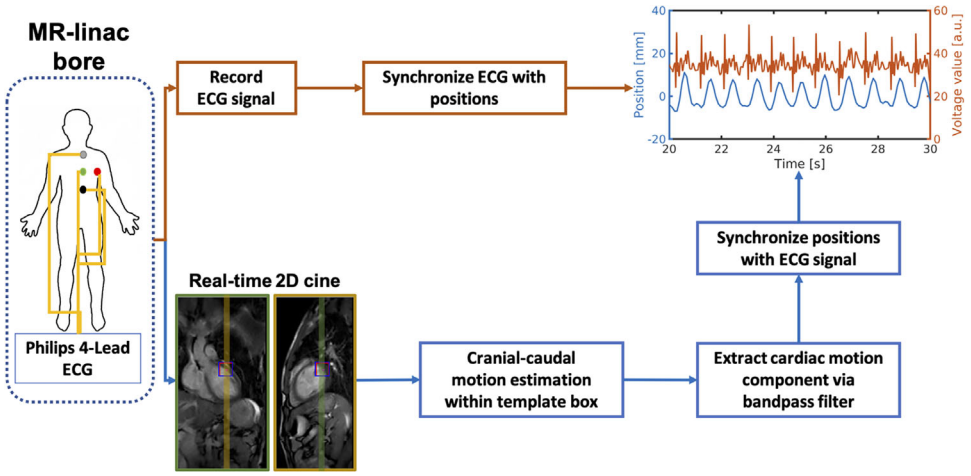

FIGURE 3 Myocardial cranial–caudal motion was estimated in the red template box using local rigid registration. The image plane positioning was indicated by the green and yellow colored borders. The obtained cardiac motion traces were synchronized with the ECG-signal recorded during the cine MRI acquisition.

triple-channel dosimetry analysis with lateral corrections using inhouse-developed software.[42,43]

The dosimetric films were rigidly registered to the static reference film using the three indents (created by the film cassette) on the corners of the films. The registered films were used to create dose difference maps and perform local gamma analyses (1%/1-mm and 2%/2-mm evaluation criteria) with respect to the static reference. For the local gamma analyses, quantified dose $\leq 10\%$ of the prescribed dose were omitted to minimize the effect of film calibration uncertainties. The GTV and PTV coverage were analyzed using dose area histograms (DAH). The dosimetric effects outside the PTV were analyzed by looking at the first and 99^{th} percentile dose differences with respect to the static reference.

2.5.2 | Gating performance evaluation

The gating performance was evaluated by calculating the residual motion (defined as the standard deviation of the motion trace during beam-on time) reduction and duty cycles (defined as the percentage of beam-on time over total treatment time) in both ECG- and MRI-based gating approaches. For the ECG-based gating workflow, the R-top detection performance was retrospectively calculated by comparing the prospectively detected R-tops with the total amount of R-tops (retrospectively detected from the log-files) during dose delivery. For the MRI-based gating workflow, the motion estimation performance was investigated by point-wise position comparison between the image-based predicted position and the phantom-reported reference positions. The mean absolute error (MAE) and root mean-squared error (RMSE) were calculated as error metrics.

2.6 | In vivo gating performance simulation

The short cine acquisition datasets were used to retrospectively estimate cardiac motion patterns in the three orthogonal directions (CC, AP, and RL) on the intersection of the acquisition planes and were aligned with their corresponding ECG signals. The obtained motion patterns and ECG signals were retrospectively processed to simulate a wide range of gating windows.

For ECG-gating simulations, the gating windows were defined per cardiac cycle. The end of each gating window was fixed at the following R-top (i.e., R_{t+1}). The duration of each gating window was increased with intervals of 20 ms and limited to the first R-top of each cardiac cycle (i.e., R_t).

For MRI-based gating simulations, the gating windows were defined starting from the lowest position over the whole motion trace. The gating windows were increased with an interval of 0.1 mm.

The duty cycle for each simulation was calculated by calculating the percentage of the total beam-on time with respect to the duration of the whole ECG/motion trace. The effect of the gating approaches was investigated by analyzing the resulting residual motion (defined as the standard deviation of the motion trace during beam-on) and beam-on duty cycle trade-off.

3 | RESULTS

3.1 | System latencies

The end-to-end latency of the ECG-based gating workflow was estimated at 78.7 ± 18.0 ms with $T_{s_{ECG}} + T_{s_{proc_{ECG}}}$ of 43.7 ± 14.6 ms and T_{gate} of 35.0 ± 10.5 ms.

TABLE 1 An overview of the effective gating efficiency. Residual motion reduction is specified relative to a 100% duty cycle (no gating).

	Mean ± SD HR [bpm]	Duty cycle [%]	Mean ± SD gating window [ms]	Residual motion [mm]	Residual motion reduction [%]
V1					
No gating	46.8 ± 3.8	100	-	3.6	-
ECG-based	47.0 ± 3.8	60.6	778.1 ± 72.7	1.4	62.5
MRI-based	46.9 ± 4.5	68.9	787.9 ± 94.1	2.0	44.7
V2					
No gating	70.1 ± 4.9	100	-	3.2	-
ECG-based	70.8 ± 5.5	47.6	409.4 ± 57.0	1.8	43.9
MRI-based	70.9 ± 5.7	50.1	467.1 ± 53.0	1.5	59.3

The end-to-end latency of the MRI-based gating workflow was estimated at 87.7 ± 11.8 ms with $T_{s_{im}} + T_{proc_{pos}}$ of 52.7 ± 5.4 ms.

3.2 | Dose delivery evaluation

3.2.1 | Gating performance evaluation

The R-top detection performance of our algorithm during the ECG-based gating experiments was evaluated. Our algorithm detected 100% of the present R-tops during the radiation delivery session for both cardiac motion traces. A constant T_d of 450 ms (trace V1) and 400 ms (trace V2) was used.

The position estimation performance during the MRI-based gating experiments was evaluated. The MAE (RMSE) of the obtained position signal with respect to the phantom-reported positions was estimated at 1.5 (2.1) mm and 1.6 (1.9) mm for V1 and V2, respectively.

The resulting effective duty cycles, average gating window duration, and corresponding residual motion for both ECG- and MRI-based gating experiments are summarized in Table 1. Note that the ratio of the mean gating window over the mean HR for the MRI-based gating experiments deviated within a range of −5.1 and 7.3 percentage-points from the reported duty cycle due to beam interruptions after inadequate circle tracking.

3.2.2 | Film dosimetry evaluation

The measured dose distribution, dose difference (with respect to a static reference delivery), and local γ-analysis maps (1%/1 mm) are shown in Figure 4. The gamma-pass rates and dose differences outside the PTV are shown in Table 2.

Local gamma analysis

The gated dose delivery scenarios were in close agreement with the static dose delivery. Local gamma pass rates with the 2%/2-mm evaluation criterion were in the range of 98.9%–100.0%. Local gamma analysis pass rates with the 1%/1 mm evaluation ranged from 70.3% to 98.3% in the film dosimetry experiments. Cardiac gating improved the gamma pass rates with a maximum of 27.3 percentage-points with respect to dose delivery without motion mitigation. Absolute difference in γ-pass rates between the ECG- and MRI-based gating scenarios were estimated at 3.5 (in favor of ECG-based gating) and 7.8 (in favor of MRI-based gating) percentage-points for the first and second trace, respectively.

Dose differences

Scaled to a full plan with 25-Gy prescription dose, a maximum median dose difference of 1.1 Gy was measured within the PTV across all gating scenarios. The dose outside the PTV was noticably altered. The dose difference maps (Figure 4) show prominent hot (83.9–87.3 mm^2) and cold spots (36.6–39.2 mm^2) at the edge of the PTV, which decrease by 93.2%–99.7% by ECG-based gating and 100% by MRI-based gating. The maximum/minimum dose differences within the hot/cold spots are shown in Table 2 per gating scenario (scaled to a full plan with 25-Gy prescription dose). ECG-based (MRI-based) gating decreased the maximum dose difference by 36.3% (51.4%) and the minimum dose difference with 45.4% (53.4%).

3.3 | In vivo gating simulation evaluation

3.3.1 | Gating simulation results

Physiological parameters from the volunteer-derived motion traces are summarized in Table 3. The residual motion as function of gating duty cycle for both ECG- and MRI-based gating approaches are shown in Figure 5 for a single volunteer data set (V1) and the results for the remaining four volunteer data sets can

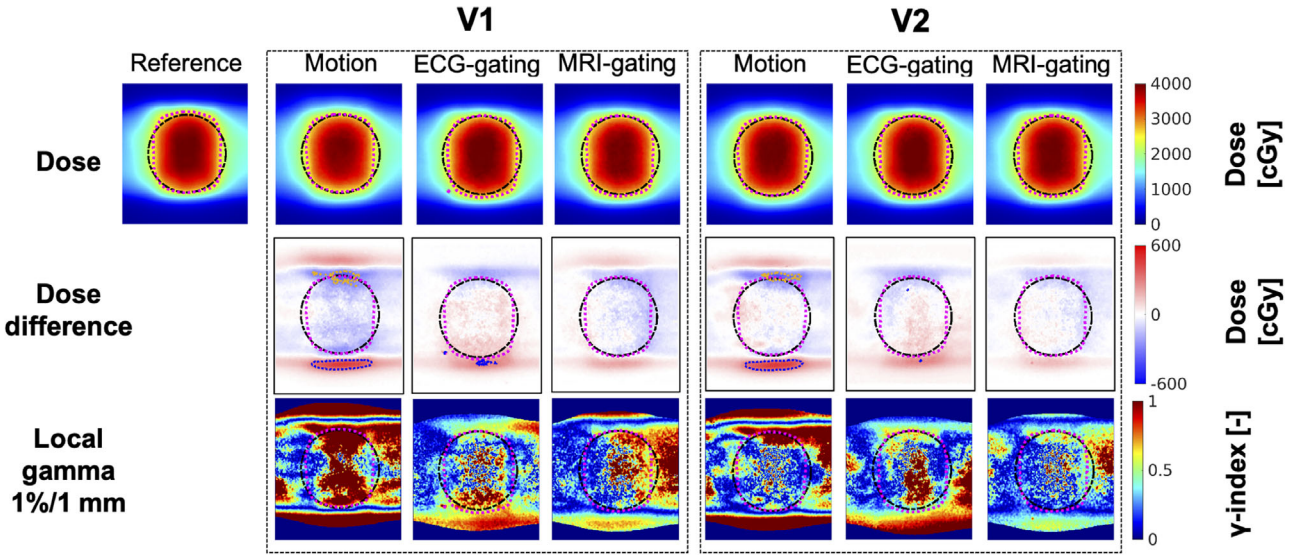

FIGURE 4 An overview of the dosimetric film results including dose distribution, dose difference, and local γ-analysis (1%/1 mm) maps. The dose levels were rescaled to a full plan with 1 × 25-Gy prescription. The prescription isodose contour is shown with the magenta-colored dashed line, while the PTV is drawn with the spherical black dashed line. In the dose difference maps, a 3-Gy isodose contour is drawn with the blue line, while the −3-Gy isodose contour is drawn with the dark yellow line.

TABLE 2 Dose differences (rescaled to full 25-Gy plan) within hot/cold spots and gamma pass rates with respect to the static reference for the film dosimetry experiments.

	Maximum dose differences		Gamma pass rates (≥ 10% PD)	
	Cold spot [Gy]	Hot spot [Gy]	1%/1 mm [%]	2%/2 mm [%]
V1				
No gating	−4.0	4.8	70.3	98.9
ECG-based	−2.5	3.3	97.6	100.0
MRI-based	−2.5	2.3	94.1	99.8
V2				
No gating	−4.1	4.8	82.0	99.8
ECG-based	−2.2	3.0	90.5	99.5
MRI-based	−1.9	2.8	98.3	100.0

TABLE 3 Physiological parameters of the invivo cardiac motion traces that were used in the in silico experiments.

	Age [years]	Mean ± SD HR [bpm]	Peak-to-peak amplitude (CC–AP–RL) [mm]	Residual motion (CC–AP–RL) [mm]
V1	26	43.8 ± 2.9	18.8–11.4–8.9	4.6–2.8–1.9
V2	26	71.0 ± 4.7	14.7–7.5–9.0	4.0–0.9–2.5
V3	27	47.1 ± 5.2	17.3–7.3–6.5	4.8–1.8–1.1
V4	26	66.1 ± 2.4	12.8–4.5–10.8	3.9–1.0–3.3
V5	43	53.0 ± 1.3	16.1–7.0–10.8	4.3–1.7–3.2

be found in the Appendix (c.f., Figure S-2). The reduction of the residual motion with respect to a 100% duty cycle was calculated at three different duty cycle percentages in each direction and is shown in Table 4. Average residual motion differences of 28, 22, and 27 percentage points were measured at a 70% duty cycle between the ECG- and MRI-based gating approaches in the CC, RL, and AP directions, respectively. Average residual motion differences between ECG- and MRI-based gating approaches were 8, 11, and 9 percentage

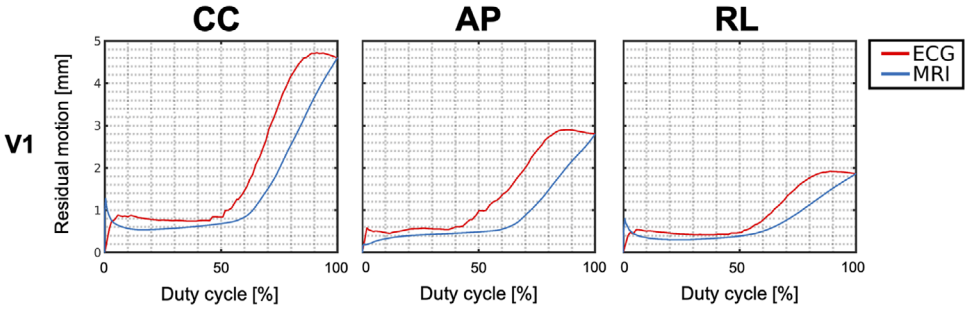

FIGURE 5 The relation between the residual motion and duty cycle is shown for the ECG- and MRI-based gating approaches in each of the orthogonal directions for a single volunteer (V1) dataset.

TABLE 4 An overview of the reduction of residual motion in comparison with the total residual motion in each orthogonal direction for a selection of duty cycle percentages.

Duty cycle	Residual motion reduction [%]		
	30%	50%	70%
	CC–AP–RL	CC–AP–RL	CC–AP–RL
V1			
ECG	84–80–78	83–65–76	39–29–30
MRI	88–85–84	85–83–79	67–69–59
V2			
ECG	81–56–79	71–48–75	14–23–20
MRI	87–68–88	74–55–79	44–36–48
V3			
ECG	76–59–50	78–59–42	36–49–18
MRI	88–76–62	85–69–55	66–60–45
V4			
ECG	77–48–79	67–41–70	20–23–22
MRI	89–63–87	74–52–77	44–40–49
V5			
ECG	85–74–73	85–69–74	31–17–29
MRI	90–79–85	86–72–78	61–48–54
Average			
ECG	80–63–72	77–56–68	28–28–24
MRI	88–74–81	81–66–74	56–51–51

points at 30% duty cycle and 4, 10, and 6 percentage points at 50% duty cycle.

4 | DISCUSSION

This is the first study in which an adaptive cardiac treatment beam-gating workflow was demonstrated using an ECG-signal as motion surrogate on an MR-linac. Cardiac motion was successfully mitigated in real-time using the ECG-signal in phantom, by-passing cardiac MRI challenges, and in silico experiments.

Our beam-gating dosimetric results showed close agreements with the static reference delivery in contrast to the dosimetric results without beam gating. Strict local gamma pass rates (min–max) of 90.5%–97.6% and 94.1%–98.3% were observed for the ECG- and MRI-based beam gating approaches using two volunteer-derived motion models, respectively, which represented an increase of 27.3 and 16.3 percentage points with respect to the unmitigated motion scenarios. We observed comparable gamma pass rate improvements when using either the ECG- or MRI-based gating approach.

A real-time workflow was developed on the Elekta Unity 1.5 T MR-linac in which the ECG-signal of the subject was received in real-time on our client PC using Philips hard- and software in a research configuration. The ECG-data had to be processed prospectively on the client PC for R-top detection and gating window determination, which was done using an in-house developed algorithm in Python. The radiation beam-gating decision was made prospectively, which allowed us to gate the radiation beam in real-time during each cardiac cycle.

An MRI-based real-time beam-gating workflow, based upon our earlier study,[27] was created with improved image streaming functionalities using ReconSocket,[37] which was used as benchmark for ECG-based cardiac motion beam gating evaluation.

Both ECG- and MRI-based beam-gating workflows are subject to system latencies. Our strategy for latency compensation differed for both methods. For our ECG-based gating approach, the latency compensation was included in our delay time, T_d, and beam-on time, T_B, determination (i.e., the latency was subtracted from our desired T_d). For our MRI-based gating approach, a linear ridge predictor model was used that predicted the cardiac position (in excellent agreement with the measured positions) allowing radiation beam-gating in each cardiac cycle.

The dose delivery time of our used cardiac SBRT plan was 26:20 min without motion mitigation when scaled to a full 1×25 Gy prescription. The ECG-based dosimetric experiments using volunteer-derived traces V1 and V2 were successfully completed achieving duty cycles of 60.6% and 47.6% resulting in dose delivery times of 43:27 and 55:26 min, respectively. With the ECG-based

gating approach, the residual motion was reduced by 62.5% and 43.9% using traces V1 and V2, respectively. The MRI-based gating experiments resulted in duty cycles of 68.9% and 50.1% using traces V1 and V2 resulting in dose delivery times of 38:13 and 52:14 min, respectively, when scaled to a full 1 × 25 Gy prescription. The residual motion was reduced with 44.7% and 59.3% using traces V1 and V2, respectively. The residual motion reduction was superior using the ECG-based gating approach in V1 with 17.8 percentage-points, while the MRI-based gating approach yielded improved residual motion reduction with 15.4 percentage-points in V2 with a higher duty cycle (+2.5 percentage-points).

The dosimetric film results show that the cardiac motion has a subtle effect on the dose deposition within the PTV using both cardiac motion traces (V1 and V2). The subtle dose difference within the GTV and PTV is mainly a result due to the slim difference (0.2–0.6 mm) between the GTV-to-PTV margin of 3 mm and the residual motion of both motion traces (c.f., Table 1). However, the experimental results have still shown that the cardiac motion has a significant effect on the dose delivery performance.

The experimental dosimetry results indicated that both ECG- and MRI-based radiation beam gating were feasible options for cardiac motion mitigation for improved dose deliveries. However, variations in both dose delivery performances were noticed. The dose delivery with trace V1 was superior using the ECG-based approach relative to the MRI-based approach, while the dose delivery with trace V2 was more successful with the MRI-based approach with respect to the ECG-based approach. It is, however, noticeable that the duty cycle was higher with the MRI-based approach, while achieving a better gating performance than using the ECG-based approach. These gating results indicated that the MRI-based gating approach allowed for superior spatial confinement of the gating window as the gating decisions were based on the actual position of the target and not a surrogate.

Additionally, gating simulations were done to evaluate the gating performance of the ECG- and MRI-based approaches with subject-derived cardiac motion traces. For beam gating, there is a clear trade-off between the chosen duty cycle and resulting residual motion. The simulation results (Table 4) show maximum residual motion reductions of 46, 20, and 45 percentage points in the CC, AP, and RL directions, respectively, when decreasing the duty cycle from 70% to 50% using the ECG-based approach. The MRI-based results indicate an additional reductions of 18, 14, and 20 percentage points in the CC, AP, and RL directions, respectively. The limited decrease is a result of improved residual motion reduction (with a maximum of 30 percentage points) at a 70% duty cycle with respect to the ECG-based gating approach, indicating a more effective spatial confinement with MRI-based beam-gating. A maximum residual motion reduction of 9% across all subjects and methodologies was obtained when decreasing the duty cycle from 50% to 30%, indicating that motion mitigation was less efficient at lower duty cycles.

In this study, we were able to demonstrate an ECG-based adaptive dose delivery workflow, but there are some aspects that require further development and/or investigation.

We deliberately decided to omit respiratory motion mitigation as the ECG-signal is a motion surrogate for cardiac motion only. Respiratory motion mitigation should be considered for free-breathing applications as consecutive breath-holds are physically demanding for VT patients. As cardiac motion is mitigated by gating, another motion mitigation approach (e.g., MLC-tracking[44]) could be considered for respiratory motion to maintain a high treatment efficiency. The combination of MLC-tracking and beam gating was experimentally demonstrated for CC motion in our previous study.[27] Respiratory MLC-tracking in 3D would be feasible by interleaved coronal/sagittal MRI due to the slower periodic respiratory motion and could be potentially compatible with ECG-based beam gating of cardiac motion.

The presence of a CIED was not investigated in this study. The utilized bSSFP cine MRI sequence is the gold standard for cardiac cine MR acquisitions due to its superior contrast-to-noise ratio with short TRs, but it is also highly sensitive to off-resonance effects.[45] Metallic and electronic implantable devices like CIEDs will heavily induce these off-resonance effects leading to banding artefacts and signal inhomogeneities. A CIED will, therefore, corrupt the MR image quality and possibly even obscure the cardiac target on the MR images in a VT patient. Alternative MRI sequences are being explored to reduce CIED-induced artefacts, such as signal loss and signal hyperintensity. Gradient-echo and spin-echo-based sequences, such as T_1-spoiled gradient echo or turbo spin echo sequences,[46,47] are less sensitive to signal-nullifying effects and can, therefore, be viable alternatives for visualizing structures that would otherwise be obscured due to CIED-induced artifacts. The presence of a CIED or any other metallic objects also disrupt the main magnetic field locally and consequentially introduces geometric distortion. Field-mapping can be used to measure the extent of geometric distortions[48,49] and, additionally, MRI sequences can case-dependently be tailored to reduce metal-induced artifacts (e.g., increasing read-out bandwidth).[50]

Utilizing the ECG-signal of the VT patient for cardiac motion mitigation might still be a feasible alternative if cardiac MRI fails due to CIED-induced artefacts. However, prior clinical cases have demonstrated that respiratory motion can be mitigated by tracking extracardiac structures,[20] which are likely to be unaffected by the effects of CIEDs.

The moving cylinder of the motion phantom moved according to a 1D motion trace. A second motion dimension was achieved by installing the motion phantom on a ramp. The ability of programming a 3D motion trace in a suitable motion phantom would be ideal as the ECG-signal could then be experimentally investigated as a 3D cardiac motion surrogate. To overcome this limitation, the development of more complex motion phantoms is desired.

Throughout the study, we estimated the center-of-gravity motion in the basal anterolateral myocardial wall of the left ventricle (which agrees with segment 6 of the 17-segment left ventricle model[40]) with a local rigid registration approach, which provides a reasonable estimate with a relatively small template (27×27 mm^2). The motion is likely the highest in this segment but is not necessarily representative of the left ventricular motion in the other segments. The motion extents in the other segments of the heart might be higher or lower depending on the patient specific anatomy and condition.[13]

During the in silico experiments, 3D motion of the basal anterolateral myocardial wall was estimated via local rigid registration by processing linearly upsampled 2D single-slice cine acquisitions that were acquired consecutively in the coronal and sagittal planes. The acquired data were sufficient to retrospectively estimate 3D motion in the orthogonal directions, but the quality of the analysis would likely to be improved in the case when 3D cardiac motion could be acquired within a single acquisition. Research studies have demonstrated the possibility to estimate 3D cardiac motion using an MRI or MR-linac, which show potential to overcome the 3D cardiac motion estimation limitation.[51,52] In a successful deployment of an MRI-based 3D cardiac motion mitigation, the real-time ECG signal acquisition could then be used as an independent sensor for dose delivery quality control during treatment. Here, the improvement of the temporal and spatial resolution of cardiac cine MRI for motion estimation is also desired. Recent studies demonstrated the achievement of a 16-fold accelerated cardiac cine MRI imaging with a spatial resolution of $1.8 \times 1.8 \times 8$ mm^3 and temporal resolution in the range of 28–34 ms using compressed sensing combined with a deep learning model.[53] However, the investigation for a hybrid (MRI + ECG) approach for 3D cardiac motion mitigation was outside the scope of this paper, but it would be desirable to achieve the same performance on the MR-linac in the future.

Obtaining a reliable ECG-signal is crucial for efficient ECG-based radiation beam gating. The ECG-signal can become distorted within the presence of the magnetic field of the MRI due to the magnetohydrodynamic effect and noise induced by rapidly switching RF fields. Additionally, in the phantom experiments, RF noise can affect the ECG-signal reliability and MR image quality since electrical cables were passed through the waveguide. In the future, adaptations to the RF-filterbox of the Unity MR-linac may be made to avoid passing electric cables through the waveguide. Alternatively, fiberoptic cables passed through the waveguide may also be used.[54] This is not an issue for clinical applications, in which ECG-signals are recorded directly from the subject/patient and transmitted wirelessly.

One of the key consequences of the magnetohydrodynamic effect is the elevated T-wave, which can compromise the true positive detection of the R-top. For radiation beam gating applications, additional fail-safe mechanisms should be applied in the R-top detection algorithm to prevent undesired radiation beam gating. In this study, no false positive R-tops were detected due to the elevated T-waves. However, a bigger study group is desired to optimize our R-top detection algorithm.

The ECG equipment should also be tested in a treatment setting (i.e., during dose delivery) to investigate the effect of radiation (scatter) on the ECG-equipment leading to potential beam treatment issues.[30] In this study, the ECG-equipment was placed outside the bore within the treatment room. During a treatment session, the ECG-equipment has to be placed close to the subject within the bore and needs to be robust during the whole treatment session.

In this study, we proposed a prototype real-time gating workflow in which we used the ECG-signal as a motion surrogate signal and conducted dosimetric experiments on healthy volunteer data to test its performance. While the technical feasibility was demonstrated successfully, we acknowledge that the clinical feasibility for VT patients should be investigated in future studies.

An effective duty cycle of 60.6% was achieved with a heart rate of 47.0 bpm, while the effective duty cycle decreased to 47.6% with a heart rate of 70.8 bpm. The effective duty cycle decreases with increasing heart rate due to the shortened quiescent phase suitable for treatment gating. Based on our experimental results, the effective duty cycle is prone to decrease below 30% with heart rates greater than 90 bpm. For such high heart rates, the ECG-gating workflow is still capable of mitigating cardiac motion, but the dose delivery time would be significantly prolonged. In this case, the practical/clinical feasibility must be questioned.

VT patients carry the risk of experiencing VT episodes during the dose delivery, therefore it is important to have an arrhythmia detection feature in our setup. In this study, the Philips MRI 4-lead ECG equipment was used that is also being used in other Philips MRI scanners during clinical scan sessions. Importantly, the MRI scanner has an arrhythmia detection feature incorporated which could be translated to use during radiation beam gating. We have, however, not explored this feature within our real-time prototype workflow, which should be done in future works for clinical feasibility purposes. Additionally, the Philips MRI scanners sample physiology-signals with a frequency of 496 Hz (with a wireless setup). A potential integration in the

low-level software environment of the Philips MRI scanners could enable an ECG-signal processing pathway similar to current implementation for MR imaging purposes. By integrating the beam-gating pathway in a similar environment, the radiation beam-gating workflow would be synchronized with MR imaging during a treatment session and, more importantly, attain higher duty cycles at higher heart rates. The patients within the eligible patient group are likely to have an ICD with additional cardiac pacing mode. The ICD is often programmed in a constant pacing mode when the patient is positioned within an MRI (often at 70 bpm, but the setting remains patient-dependent) based on instructions from the CIED manufacturer or responsible medical staff to minimize the risk of an arrhythmia episode occurrence.[55]

5 | CONCLUSION

This work demonstrated the feasibility of using an ECG-signal to gate the radiation beam in real-time reducing cardiac motion-induced dosimetric uncertainties. The dose deposition was greatly improved in presence of cardiac motion using the ECG-signal and its performance was comparable with MRI-based gating, while by-passing MR imaging challenges for cardiac motion mitigation. The dose delivery performance using the ECG-signal as a beam gating surrogate depends on the combination with its corresponding motion trace, but also on the true positive R-top detection rate, given gating conditions and fail-safe mechanisms. Further research with a wider variety of ECG and motion traces is required to improve the robustness of the demonstrated ECG-based gating approach. With these improvements, the clinical feasibility should then be tested by using VT patient data.

ACKNOWLEDGMENTS

M. F. Fast and P. Uijtewaal acknowledge funding by the Dutch Research Council (NWO) through project no. 17 515 (BREATHE EASY). This study received research support from Elekta AB, Philips Healthcare, and IBA Quasar.

CONFLICT OF INTEREST STATEMENT

The authors declare no conflicts of interest.

REFERENCES

1. Soejima K, Suzuki M, Maisel WH, et al. Catheter ablation in patients with multiple and unstable ventricular tachycardias after myocardial infarction: short ablation lines guided by reentry circuit isthmuses and sinus rhythm mapping. *Circulation*. 2001;104:664-669.
2. Aliot EM, Stevenson WG, Almendral-Garrote JM, et al. EHRA/HRS expert consensus on catheter ablation of ventricular arrhythmias. *Heart Rhythm*. 2009;6:886-933.
3. Knybel L, Cvek J, Neuwirth R, et al. Real-time measurement of ICD lead motion during stereotactic body radiotherapy of ventricular tachycardia. *Rep Pract Oncol Radiother*. 2021;26:128-137.
4. Kahle AK, Jungen C, Alken FA, et al. Management of ventricular tachycardia in patients with ischaemic cardiomyopathy: contemporary armamentarium. *EP Europace*. 2022;24:538-551.
5. Sharp AJ, Mak R, Zei PC. Noninvasive cardiac radioablation for ventricular arrhythmias. *Curr Cardiovasc Risk Rep*. 2019;13:1.
6. Grehn M, Mandija S, Miszczyk M, et al. STereotactic Arrhythmia Radioablation (STAR): the Standardized Treatment and Outcome Platform for Stereotactic Therapy Of Re-entrant tachycardia by a Multidisciplinary consortium (STOPSTORM.eu) and review of current patterns of STAR practice in Europe. *EP Europace*. 2023;25:euac238.
7. Cvek J, Neuwirth R, Knybel L, et al. Cardiac radiosurgery for malignant ventricular tachycardia. *Cureus*. 2014;6(7):e190.
8. Loo BW, Soltys SG, Wang L, et al. Stereotactic ablative radiotherapy for the treatment of refractory cardiac ventricular arrhythmia. *Circ: Arrhythm Electrophysiol*. 2015;8:748-750.
9. Zei PC, Soltys S. Ablative radiotherapy as a noninvasive alternative to catheter ablation for cardiac arrhythmias. *Current Cardiology Reports*. 2017;19(9):79.
10. Miszczyk M, Jadczyk T, Gołba K, et al. Clinical evidence behind stereotactic radiotherapy for the treatment of ventricular tachycardia (STAR)–a comprehensive review. *J Clin Med Res*. 2021;10(6):1238.
11. Siedow M, Brownstein J, Prasad RN, et al. Cardiac radioablation in the treatment of ventricular tachycardia. *Clin Transl Radiat Oncol*. 2021;31:71-79.
12. Shangguan W, Xu G, Wang X, et al. Stereotactic radiotherapy: an alternative option for refractory ventricular tachycardia to drug and ablation Therapy. *J Clin Med Res*. 2022;11(12):3549.
13. Stevens RR, Hazelaar C, Fast MF, et al. Stereotactic Arrhythmia Radioablation (STAR): assessment of cardiac and respiratory heart motion in ventricular tachycardia patients – a STOPSTORM.eu consortium review. *Radiother Oncol*. 2023;188:109844.
14. Darby SC, Ewertz M, McGale P, et al. Risk of ischemic heart disease in women after radiotherapy for breast cancer. *N Engl J Med*. 2013;368:987-998.
15. McWilliam A, Kennedy J, Hodgson C, Vasquez Osorio E, Faivre-Finn C, Herk M. Radiation dose to heart base linked with poorer survival in lung cancer patients. *Eur J Cancer*. 2017;85:106-113.
16. van der Pol LH, Hackett SL, Hoesein FAM, et al. On the feasibility of cardiac substructure sparing in magnetic resonance imaging guided stereotactic lung radiotherapy. *Med Phys*. 2023;50:397-409.
17. Cuculich PS, Schill MR, Kashani R, et al. Noninvasive cardiac radiation for ablation of ventricular tachycardia. *N Engl J Med*. 2017;377:2325-2336.
18. Robinson CG, Samson PP, Moore KM, et al. Phase I/II Trial of electrophysiology-guided noninvasive cardiac radioablation for ventricular tachycardia. *Circulation*. 2019;139:313-321.
19. Lydiard S, Blanck O, Hugo G, O'Brien R, Keall P. A review of cardiac radioablation (CR) for arrhythmias: procedures, technology, and future opportunities. *Int J Radiat Oncol Biol Phys*. 2021;109:783-800.
20. Mayinger M, Kovacs B, Tanadini-Lang S, et al. First magnetic resonance imaging-guided cardiac radioablation of sustained ventricular tachycardia. *Radiother Oncol*. 2020;152:203-207.
21. Pomp J, van Asselen B, Tersteeg RH, et al. Sarcoma of the heart treated with stereotactic MR-guided online adaptive radiation therapy. *Case Rep Oncol*. 2021;14:453-458.
22. Noyan A, Yavas G, Efe E, Arslan G, Yavas C, Onal C. Cardiac angiosarcoma treated with 1.5 Tesla MR-guided adaptive stereotactic body radiotherapy – case report and review of the literature. *Int J Surg Case Rep*. 2022;98:107521.

23. Batumalai V, Carr M, Jameson M, et al. MR-Linac guided adaptive stereotactic ablative body radiotherapy for recurrent cardiac sarcoma with mitral valve bioprosthesis – a case report. *J Med Radiat Sci*. 2023;70:199-205.
24. Kensen CM, Janssen TM, Betgen A, et al. Effect of intrafraction adaptation on PTV margins for MRI guided online adaptive radiotherapy for rectal cancer. *Radiat Oncol*. 2022;17(1):110.
25. Willigenburg T, Zachiu C, Bol GH, et al. Clinical application of a sub-fractionation workflow for intrafraction re-planning during prostate radiotherapy treatment on a 1.5 Tesla MR-Linac: a practical method to mitigate intrafraction motion. *Radiother Oncol*. 2022;176:25-30.
26. Corradini S, Bestenbostel R, Romano A, et al. MR-guided stereotactic body radiation therapy for primary cardiac sarcomas. *Radiat Oncol*. 2021;16(1):60.
27. Akdag O, Borman PTS, Woodhead P, et al. First experimental exploration of real-time cardiorespiratory motion management for future stereotactic arrhythmia radioablation treatments on the MR-linac. *Phys Med Biol*. 2022;67(6):065003.
28. Horwood L, Attili A, Luba F, et al. Magnetic resonance imaging in patients with cardiac implanted electronic devices: focus on contraindications to magnetic resonance imaging protocols. *Europace*. 2016;19:euw122.
29. Maass AH, Hemels MEW, Allaart CP. Magnetic resonance imaging in patients with cardiac implantable electronic devices. *Neth Heart J*. 2018;26:584-590.
30. Miften M, Mihailidis D, Kry SF, et al. Management of radiotherapy patients with implanted cardiac pacemakers and defibrillators: A report of the AAPM TG-203 †. *Med Phys*. 2019;46(12).
31. Peschke E, Ulloa P, Jansen O, Hoevener JB. Metallic implants in MRI – hazards and imaging artifacts. *Rofo Fortschr Geb Rontgenstr Neuen Bildgeb Verfahr*. 2021;193:1285-1293.
32. Vigen KK, Reeder SB, Hood MN, et al. Recommendations for imaging patients with cardiac implantable electronic devices (CIEDs). *J Magn Reson Imaging*. 2021;53:1311-1317.
33. Poon J, Kohli K, Deyell MW, et al. Technical Note: Cardiac synchronized volumetric modulated arc therapy for stereotactic arrhythmia radioablation – proof of principle. *Med Phys*. 2020;47:3567-3572.
34. Reis CQM, Robar JL. Evaluation of the feasibility of cardiac gating for SBRT of ventricular tachycardia based on real-time ECG signal acquisition. *J Appl Clin Med Phys*. 2023;24(2):e13814.
35. Akdag O, Mandija S, Van Lier AL, et al. Feasibility of cardiac-synchronized quantitative T1 and T2 mapping on a hybrid 1.5 Tesla magnetic resonance imaging and linear accelerator system. *Phys Imaging Radiat Oncol*. 2022;21:153-159.
36. Pan J, Tompkins WJ. A real-time QRS detection algorithm. *IEEE Trans Biomed Eng*. 1985;BME-32:230-236.
37. Borman PTS, Raaymakers BW, Glitzner M. ReconSocket: a low-latency raw data streaming interface for real-time MRI-guided radiotherapy. *Phys Med Biol*. 2019;64(18):185008.
38. Uijtewaal P, Borman PT, Woodhead PL, Hackett SL, Raaymakers BW, Fast MF. Dosimetric evaluation of MRI-guided multi-leaf collimator tracking and trailing for lung stereotactic body radiation therapy. *Med Phys*. 2021;48:1520-1532.
39. Krauss A, Nill S, Oelfke U. The comparative performance of four respiratory motion predictors for real-time tumour tracking. *Phys Med Biol*. 2011;56:5303-5317.
40. Cerqueira MD, Weissman NJ, Dilsizian V, et al. Standardized myocardial segmentation and nomenclature for tomographic imaging of the heart. *Circulation*. 2002;105:539-542. eprint: https://www.ahajournals.org/doi/pdf/10.1161/hc0402.102975
41. Akdag O, Mandija S, Borman PT, Alberts E, Fast MF. Feasibility of free breathing real-time cine-MRI for MR-guided cardiac radioablation on the Unity MR-linac. In: Proceedings of the International Society for Magnetic Resonance in Medicine. Vol. 29. 2021:4014.
42. Micke A, Lewis DF, Yu X. Multichannel film dosimetry with nonuniformity correction: multichannel film dosimetry with nonuniformity correction. *Med Phys*. 2011;38:2523-2534.
43. Li Y, Chen L, Zhu J, Liu X. The combination of the error correction methods of GAFCHROMIC EBT3 film. *PLOS ONE*. 2017;12(7):e0181958.
44. Keall PJ, Sawant A, Berbeco RI, et al. AAPM Task Group 264: The safe clinical implementation of MLC tracking in radiotherapy. *Med Phys*. 2021;48(5):e44-e64.
45. Scheffler K, Lehnhardt S. Principles and applications of balanced SSFP techniques. *Eur Radiol*. 2003;13:2409-2418.
46. Stojanovska J, Runge M, Mahani MG, et al. Cardiac MRI for patients with cardiac implantable electronic devices. *AJR Am J Roentgenol*. 2020;215:374-381.
47. Holtstiege V, Meier C, Bietenbeck M, et al. Clinical experience regarding safety and diagnostic value of cardiovascular magnetic resonance in patients with a subcutaneous implanted cardioverter/defibrillator (S-ICD) at 1.5 T. *J Cardiovasc Magn Reson*. 2020;22(1):35.
48. Keesman R, van der Bijl E, Janssen TM, Vijlbrief T, Pos FJ, van der Heide UA. Clinical workflow for treating patients with a metallic hip prosthesis using magnetic resonance imaging-guided radiotherapy. *Phys Imaging Radiat Oncol*. 2020;15:85-90.
49. van Lier ALHMW, Meijers LTC, Phillippens MEP, et al. Geometrical imaging accuracy, image quality and plan quality for prostate cancer treatments on a 1.5 T MRLinac in patients with a unilateral hip implant. *Phys Med Biol*. 2021;66(20):205013.
50. Rajiah P, Kay F, Bolen M, Patel AR, Landeras L. Cardiac magnetic resonance in patients with cardiac implantable electronic devices: challenges and solutions. *J Thorac Imaging*. 2020;35(1):W1-W17.
51. Ipsen S, Blanck O, Lowther NJ, et al. Towards real-time MRI-guided 3D localization of deforming targets for non-invasive cardiac radiosurgery. *Phys Med Biol*. 2016;61:7848-7863.
52. Huttinga NRF, Akdag O, Fast MF, et al. Real-time myocardial landmark tracking for MRI-guided cardiac radio-ablation using Gaussian Processes. *Phys Med Biol*. 2023;68(14):145001.
53. Yoon S, Nakamori S, Amyar A, et al. Accelerated cardiac MRI cine with use of resolution enhancement generative adversarial inline neural network. *Radiology*. 2023;307(5):e222878.
54. Jackson E, Bronskill M, Drost D, et al. *Acceptance Testing and Quality Assurance Procedures for Magnetic Resonance Imaging Facilities*. Technical Report. AAPM; 2010.
55. Indik JH, Gimbel JR, Abe H, et al. 2017 HRS expert consensus statement on magnetic resonance imaging and radiation exposure in patients with cardiovascular implantable electronic devices. *Heart Rhythm*. 2017;14(7):e97-e153.

SUPPORTING INFORMATION

Additional supporting information can be found online in the Supporting Information section at the end of this article.

How to cite this article: Akdag O, Borman PTS, Mandija S, et al. Experimental demonstration of real-time cardiac physiology-based radiotherapy gating for improved cardiac radioablation on an MR-linac. *Med Phys*. 2024;51:2354–2366. https://doi.org/10.1002/mp.17024